European Conference on Computational Fluid Dynamics
ECCOMAS CFD 2006
P. Wesseling, E. Oñate and J. Périaux (Eds)

INFLUENCE OF THE GROUP POSITIONING OF CYLINDERS ON THE WIND PRESSURE DISTRIBUTION IN THE POST-CRITICAL REGIME

David Dooms, Guido De Roeck and Geert Degrande

Katholieke Universiteit Leuven, Department of Civil Engineering
Kasteelpark Arenberg 40, B-3001 Leuven, Belgium
e-mail: David.Dooms@bwk.kuleuven.be
web page: http://www.kuleuven.be/bwm

Key words: Circular cylinder, Cylinder groups, Post-critical flow, Pressure coefficient

Abstract. *In order to estimate the wind loads on circular cylindrical shell structures, the pressure coefficient as a function of the Reynolds number is given for an isolated cylinder in Eurocode 1 - Part 2-4 : Actions on structures - Wind actions. As cylinders are often placed in groups and the configuration of these groups largely influences the pressure distribution around the cylinders, a computation of the wind flow provides a more realistic estimation of the pressure coefficients.*

First, the transient 2D turbulent air flow around a single cylinder at a Reynolds number of 1.24×10^7 is computed using the SST turbulence model and the results are compared with the pressure coefficients in Eurocode 1 and with experimental data. The minimum pressure coefficient is underestimated, while the base pressure coefficient is slightly overestimated.

Unsteady simulations are performed for the flow around a group of 2 by 2 and of 8 by 5 cylinders. Vortex shedding occurs both from the group as a whole, and from individual cylinders. The group configuration drastically changes the time-averaged pressure distribution around the cylinders. High values of suction are present at the location of the small gaps between the cylinders and upstream of the separation points of the cylinders on the side corners of the groups. The cylinders at the borders of the groups experience high drag or lift forces, while these forces are considerably lower in the middle of the group.

1 INTRODUCTION

Circular cylindrical shell structures are widely used in civil engineering as silos, chimneys and water towers. The use of high tensile strength aluminium has resulted in slender structures that are more perceptible to wind induced ovalling oscillations, where the cross section deforms as a shell without bending deformation of the longitudinal axis of symmetry. During a storm in October 2002, ovalling was observed on several empty silos of a group consisting of forty silos in the port of Antwerp. Similar cases indicate that storm damage is mainly located on silos on the corners of the group.

In order to estimate the wind loads on such structures, the pressure coefficient for a circular cylinder as a function of the Reynolds number is given in *Eurocode 1 - Part 2-4 : Actions on structures - Wind actions*[1]. As silos are often placed in groups and the configuration of these groups largely influences the pressure distribution around the cylinders, a computation of the wind flow provides a more realistic estimation of the pressure coefficients. This model will be used in a later stage for a coupled numerical analysis of the wind flow around the structure that predicts the onset velocity of ovalling.

First, the 2D incompressible turbulent flow around a single cylinder at $\mathrm{Re} = 1.24 \times 10^7$ is computed using the Shear Stress Transport turbulence model[2] of Ansys CFX[3], a finite volume code. The results are compared with the pressure coefficients of Eurocode 1 and with experimental data[4]. The computations are performed for two different meshes, one where the nodes next to the cylinder surface are situated in the logarithmic layer and one where these nodes are situated in the viscous sublayer.

Next, the effect of the configuration of groups of cylinders is studied for a 2 by 2 and a 8 by 5 group using transient computations.

2 TURBULENT AIR FLOW AROUND A SINGLE CYLINDER

In all computations air with a density $\rho = 1.25\,\mathrm{kg/m^3}$ and a dynamic viscosity $\mu = 1.76 \times 10^{-5}\,\mathrm{Pa\,s}$ is used. The mean wind velocity at a height of $z = 30\,\mathrm{m}$ for terrain category II[1] is equal to $v_m = 31.84\,\mathrm{m/s}$. At the inlet, a turbulent kinetic energy $k = 0.1521\,\mathrm{m^2/s^2}$ and a turbulent dissipation rate $\varepsilon = 0.0053929\,\mathrm{m^2/s^3}$ are imposed, which corresponds to a turbulence intensity $I = \sqrt{\frac{2}{3}k}/v_m = 1.00\%$.

The cylinders have a diameter $D = 5.5\,\mathrm{m}$, which results in a Reynolds number $\mathrm{Re} = Dv_m/\nu = 1.24 \times 10^7$. As the Reynolds number is larger than $\mathrm{Re} = 3.5 - 6 \times 10^6$, the regime of the flow around the cylinder is post-critical[4]. The wake and the shear layers are fully turbulent and the boundary layers become fully turbulent prior to separation. In the boundary layers, the transition from laminar to turbulent flow takes place between the stagnation and the separation point. In the post-critical regime, regular vortex shedding reappears, while it was absent at lower Reynolds numbers.

The pressure coefficient is a dimensionless expression for the pressure at the cylinder's surface:

$$C_p = \frac{p - p_f}{\frac{\rho v_f^2}{2}} \tag{1}$$

where p_f and v_f are the free stream pressure and velocity, respectively. Eurocode 1[1] describes the pressure coefficient as a function of the angle for $\mathrm{Re} = 10^7$. At the stagnation point, the pressure coefficient is equal to 1. The minimum value of the pressure coefficient $C_p^{\min}$ equals -1.5 at an angle of 75°. The boundary layer separates at 105°. After separation, the base pressure coefficient C_p^b is constant and equal to -0.8. Zdravkovich[4] gives an overview of available experimental data. There is a lack of detailed experimental data at post-critical Reynolds numbers, while available data show considerable scatter,

which may be explained by the high sensitivity of the flow to perturbations due to surface roughness and free-stream turbulence. In figures 2 and 5, the range of the available experimental data for the pressure coefficients at Reynolds numbers from 0.73×10^7 to 3.65×10^7 is plotted in light grey at the background.

2.1 Eddy viscosity turbulence models

Various eddy viscosity turbulence models are implemented in CFX. The Reynolds stress tensor $\overline{v_i' v_j'}$ of the Reynolds Averaged Navier-Stokes (RANS) equations, where the prime indicates the fluctuating part of the velocities and the overline denotes averaging, is split in its isotropic $\frac{2}{3}k$ and anisotropic part:

$$\overline{v_i' v_j'} = \frac{2}{3} k \delta_{ij} - \nu_t \left(\frac{\partial \overline{v_i}}{\partial x_j} + \frac{\partial \overline{v_j}}{\partial x_i} \right) \tag{2}$$

The turbulent kinetic energy is equal to $k = \frac{1}{2}\overline{v_i'^2}$. The anisotropic part is modelled by means of the turbulent kinetic viscosity and the mean strain rate tensor. The turbulent kinetic viscosity is expressed as a function of the turbulent kinetic energy k and the turbulent energy dissipation ε for the standard k-ε model and as a function of the turbulent kinetic energy k and the turbulent frequency ω for the k-ω model. Two additional transport equations are solved for every node in order to obtain k and ε or ω.

The Shear Stress Transport (SST)[2] turbulence model combines the robust and accurate formulation of the k-ω model in the near wall region with the free stream independence of the k-ε model in the outer part of the boundary layer through a blending function. It is suited to predict the onset and amount of separation under adverse pressure gradients and produces the best results of all turbulence models in CFX for a steady computation of the flow around a cylinder[5]. Therefore, it is used in all subsequent computations.

2.2 Problem domain, mesh refinement and wall functions

The boundaries should be sufficiently far from the region close to the cylinder where the accuracy of solution is important. In literature[6,7], a distance of at least $8D$ is suggested for the inlet and the lateral boundaries and a distance of $22.5D$ for the outlet, with D the diameter of the cylinder. Here, a distance of $9D$ is adopted for the inlet and the lateral boundaries and $30D$ for the outlet. Results on a larger problem domain, where the inlet and the lateral boundaries are located at $12D$ and the outlet at $40D$, are comparable.

Far away from the cylinder wall, an unstructured mesh, consisting of triangles, is used. Close to the cylinder wall and in the wake of the cylinder, the mesh is structured and consists of quadrilaterals. The simulations are performed on two different meshes. The meshes differ only in the near-wall region. For mesh A, the nodes next to the cylinder wall are placed in the logarithmic law region, where a logarithmic relation exists between the dimensionless wall distance $y^+ = v_\tau y/\nu$ and the dimensionless velocity $v^+ = v/v_\tau$, where $v_\tau = \sqrt{\tau_w/\rho}$ is the friction velocity, y the wall distance and τ_w the wall shear stress:

$$v^+ = \frac{1}{\kappa} \ln y^+ + B \tag{3}$$

y^+ can be considered as a local Reynolds number, which describes the relative importance of viscous and turbulent processes. The von Karman constant κ is equal to 0.41 and B is equal to 5.2. In the outer layer ($y^+ > 50$), direct effects of the viscosity on the main flow are negligible. Nevertheless, the region of validity of the logarithmic law can be extended to $y^+ > 30$. Mesh A consists of 53530 elements and 90798 nodes. The dimensionless wall distance y^+ of the nodes next to the cylinder wall varies from 0 at the stagnation points to 220 at time 4.68 s (figure 1a). In practice, so-called wall functions apply the logarithmic law as boundary conditions on the nodes next to the cylinder wall.

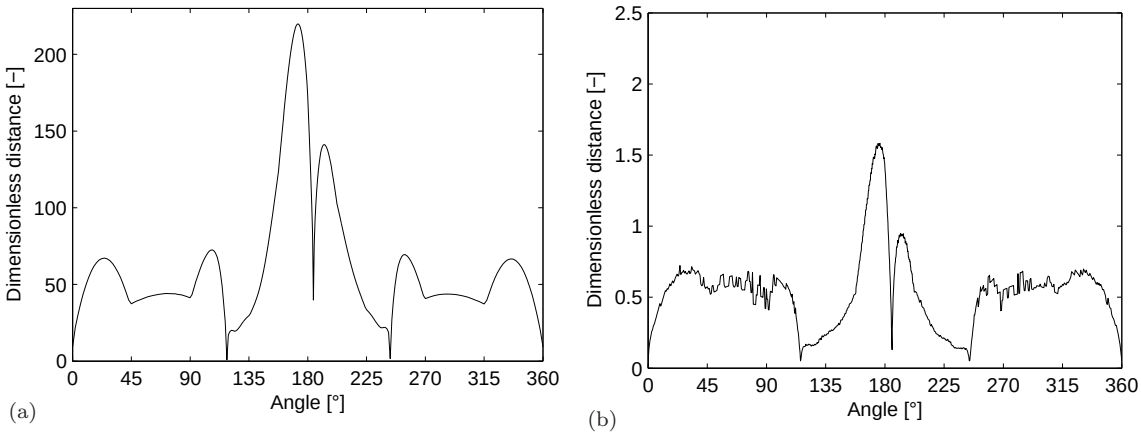

Figure 1: Dimensionless distance y^+ of the nodes next to the cylinder wall as a function of the angle θ for (a) mesh A and (b) mesh B for a single cylinder.

For mesh B, the node next to the cylinder wall is located in the viscous sublayer ($y^+ < 5$), where viscosity effects dominate and a linear relation exists between v^+ and y^+:

$$v^+ = y^+ \tag{4}$$

Ideally, five nodes are located in the viscous sublayer or $y^+ \approx 1$ for the node next to the cylinder wall. Mesh B consists of 109387 elements and 203044 nodes. The dimensionless wall distance y^+ of the nodes next to the cylinder wall is smaller than 1.6 at time 4.765 s (figure 1b).

Figure 2 shows that the mesh refinement next to the wall has only a small influence on the pressure coefficient.

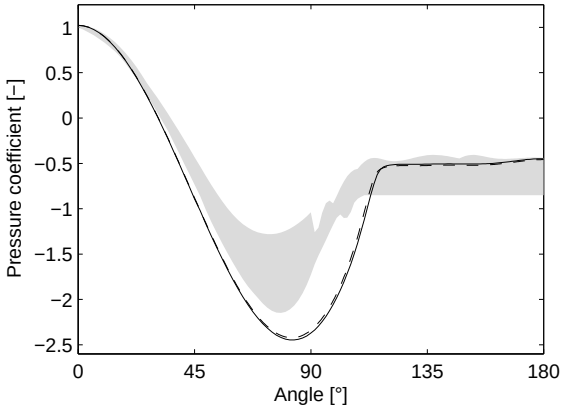

Figure 2: Influence of the mesh refinement on the pressure coefficient for a single cylinder : mesh A (solid line) and mesh B (dashed line).

2.3 Unsteady computation

In the post-critical regime regular vortex shedding is present, which demands an unsteady RANS computation[8]. The vortex shedding frequency f_{vs} is described by the dimensionless Strouhal number:

$$\mathrm{St} = \frac{f_{vs} D}{v_m} \tag{5}$$

For flows with $\mathrm{Re} \approx 10^7$, experimental values for the Strouhal number[4] range from 0.27 to 0.32. Eurocode 1 suggests a constant value of 0.2, independent of the Reynolds number.

The transient solution is integrated by the second order backward Euler scheme with a time step $\Delta t = 0.005\,\mathrm{s}$, which corresponds to approximately 100 time steps per vortex shedding period. Within every time step, 5 iterations are performed to obtain a converged solution. The computed time window corresponds to ten vortex shedding periods. For mesh A, 937 time steps are computed, which results in a time window of 4.68 s. The vortex shedding frequency is identified as 2.13 Hz, which corresponds to a Strouhal number of 0.37. For mesh B, 954 time steps are computed, which results in a time window of 4.765 s. The vortex shedding frequency is identified as 2.10 Hz, which corresponds to a Strouhal number of 0.36. The vortex shedding frequencies and Strouhal numbers are quite inaccurate since the frequency resolution $\Delta f = 1/T = 0.21\,\mathrm{Hz}$ is low. For a more accurate estimation, more time steps should be computed.

Figure 3 shows the time history and the frequency content of the pressure in a point at the cylinder's surface for mesh B. The vortex shedding frequency and some higher harmonics are clearly visible in the frequency content.

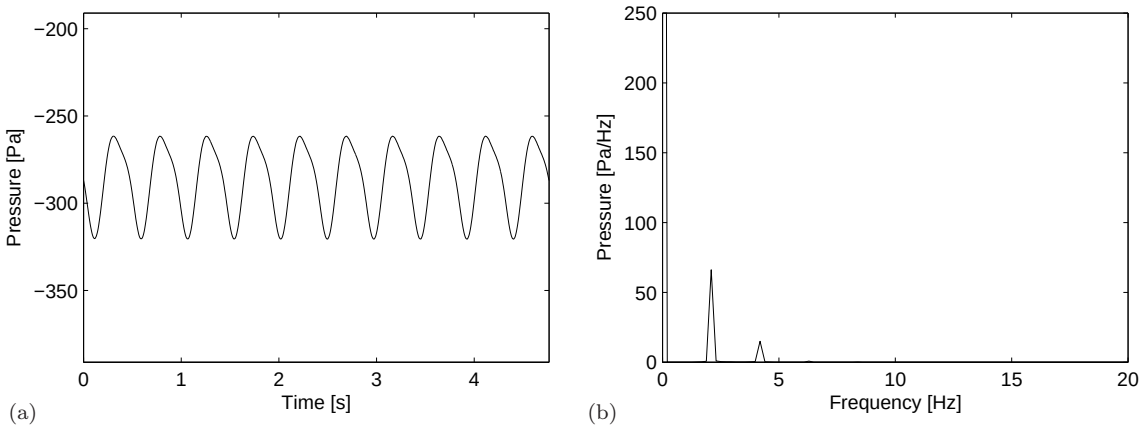

Figure 3: (a) Time history and (b) frequency content of the pressure in a point at the cylinder's surface for a single cylinder using mesh B.

Figure 4 shows the time average and the standard deviation of the pressure p. The stagnation pressure at the windward side and the suction in the wake are clearly visible. The largest time variations of the pressure occur in the wake.

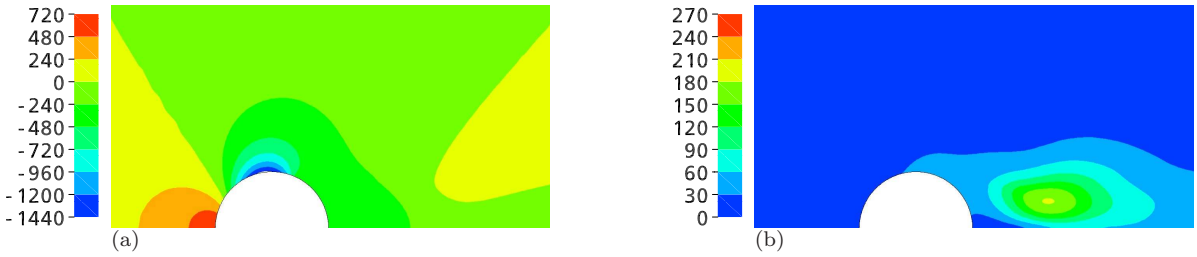

Figure 4: (a) Time average and (b) standard deviation of the pressure p for a single cylinder using mesh B.

Figure 5 compares the time-averaged pressure coefficient $\overline{C_p}$ of the transient computation with experimental data. The maxima and minima of the pressure coefficient during the transient computation are depicted as well. The time average of the transient computation predicts a too low minimum pressure coefficient $\overline{C_p}^{\min}$, while the base pressure coefficient $\overline{C_p}^{b}$ is quite high.

The drag coefficient $\overline{C_d} = \int_0^{2\pi} \overline{C_p} \cos\alpha d\alpha$ is, according to Eurocode 1, equal to 0.72 for a smooth surface ($k/b = 10^{-5}$). Drag coefficients derived from the experimental pressure coefficients vary from 0.45 to 0.73. The computations using mesh A and mesh B predict respectively 0.35 and 0.36, which are underestimations.

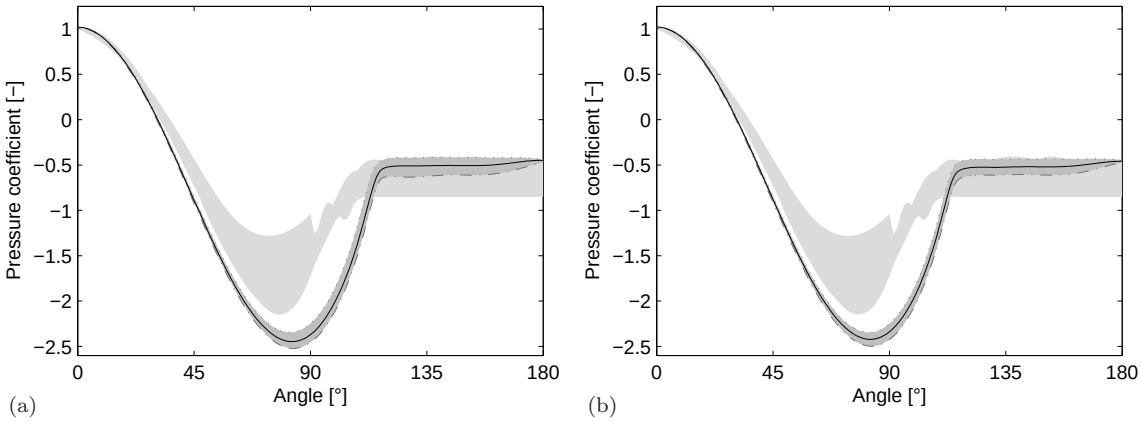

Figure 5: Comparison of the time average (solid line), minimum (dash-dotted line) and maximum (dotted line) of the pressure coefficient with experimental data for a single cylinder using (a) mesh A and (b) mesh B.

The adverse pressure recovery $\overline{\mathrm{APR}} = \overline{C_p}^b - \overline{C_p}^{\min}$ is, according to Eurocode 1, equal to 0.7, although experimental data show that it varies from 1.0 to 1.5. The computations using mesh A and mesh B predict respectively 2.00 and 1.96, which are overestimations.

3 TURBULENT AIR FLOW AROUND A GROUP OF CYLINDERS

In this section the turbulent air flow around a group of cylinders is studied. The flow around two configurations is computed: a group of 2 by 2 cylinders and a group of 8 by 5 cylinders, as in the port of Antwerp. The gaps between two neighbouring cylinders are 30 cm wide. The ratio of the distance T between the cylinder centers to the cylinder diameter is $T/D = 5.8/5.5 = 1.0545$. The angle α (figure 6) between the wind flow direction and the cylinder group is equal to 30 degrees for both configurations.

The lateral boundaries in the model are located at a distance of 9 times the projected width of the group, the inlet at a distance of 9 times the projected depth of the group and the outlet at a distance of 30 times the projected depth of the group. A smaller problem domain would probably not influence the results near the cylinders, but the number of elements in the far field is anyhow negligible to the number of elements next to the group.

3.1 2 by 2 group

Figure 6 shows a detail of the mesh near the group. The mesh consists of 201184 elements and 243348 nodes.

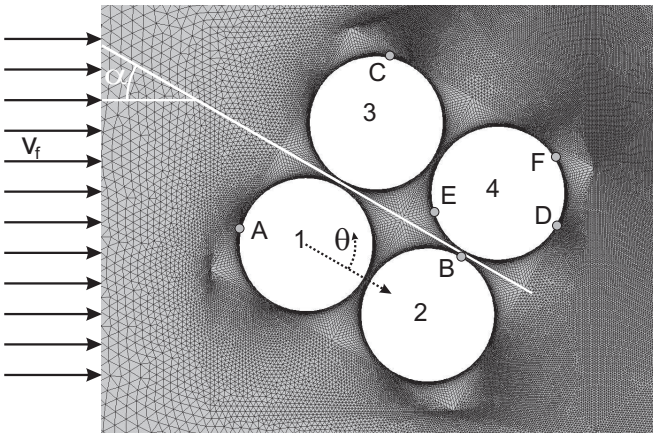

Figure 6: Detail of the mesh for the 2 by 2 cylinder group.

The transient solution is integrated with a time step $\Delta t = 0.005\,\mathrm{s}$. Maximum 10 iterations are performed within every time step to obtain a converged solution. 2965 time steps are computed, which results in a time window of 14.820 s.

Figure 7 shows the dimensionless distance y^+ of the nodes next to the cylinder wall as a function of the angle θ at time $t = 14.820\,\mathrm{s}$ of the four cylinders. Most points lie within the region where the logarithmic law is valid.

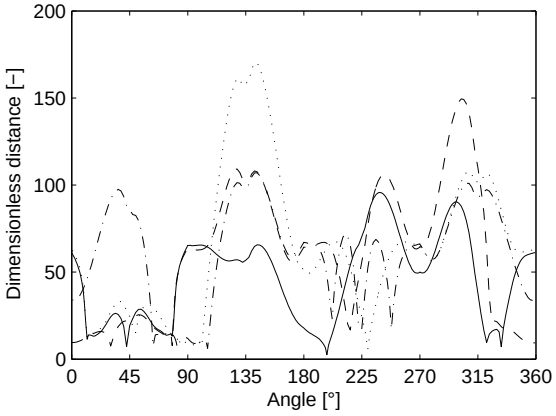

Figure 7: Dimensionless distance y^+ of the nodes next to the cylinder wall as a function of the angle θ for cylinder 1 (solid line), 2 (dashed line), 3 (dotted line) and 4 (dash-dotted line) of the 2 by 2 group.

Figure 8 shows the time history and the frequency content between $t = 7.385\,\mathrm{s}$ and $t = 14.820\,\mathrm{s}$ of the pressure at a small gap (B) and in the middle of the group (E), as indicated in figure 6. At the stagnation points, the pressure is constant in time. The largest variation of the pressure occurs at the small gaps and at the separation points. The dominant peak in the frequency content at 0.67 Hz corresponds to a Strouhal number of 0.28, using the projected width 13.42 m of the group as a characteristic diameter. In the middle of the group and in the wake, higher harmonics are clearly present in the pressure time history. From the third peak in the frequency content at 2.03 Hz, a Strouhal number of 0.35 is derived using the cylinder diameter as a characteristic diameter. Generally, time variations of the pressure are larger at the leeward side of the cylinder group. The vortex shedding frequencies and Strouhal numbers are quite inaccurate since the frequency resolution $\Delta f = 1/T = 0.13\,\mathrm{Hz}$ is low.

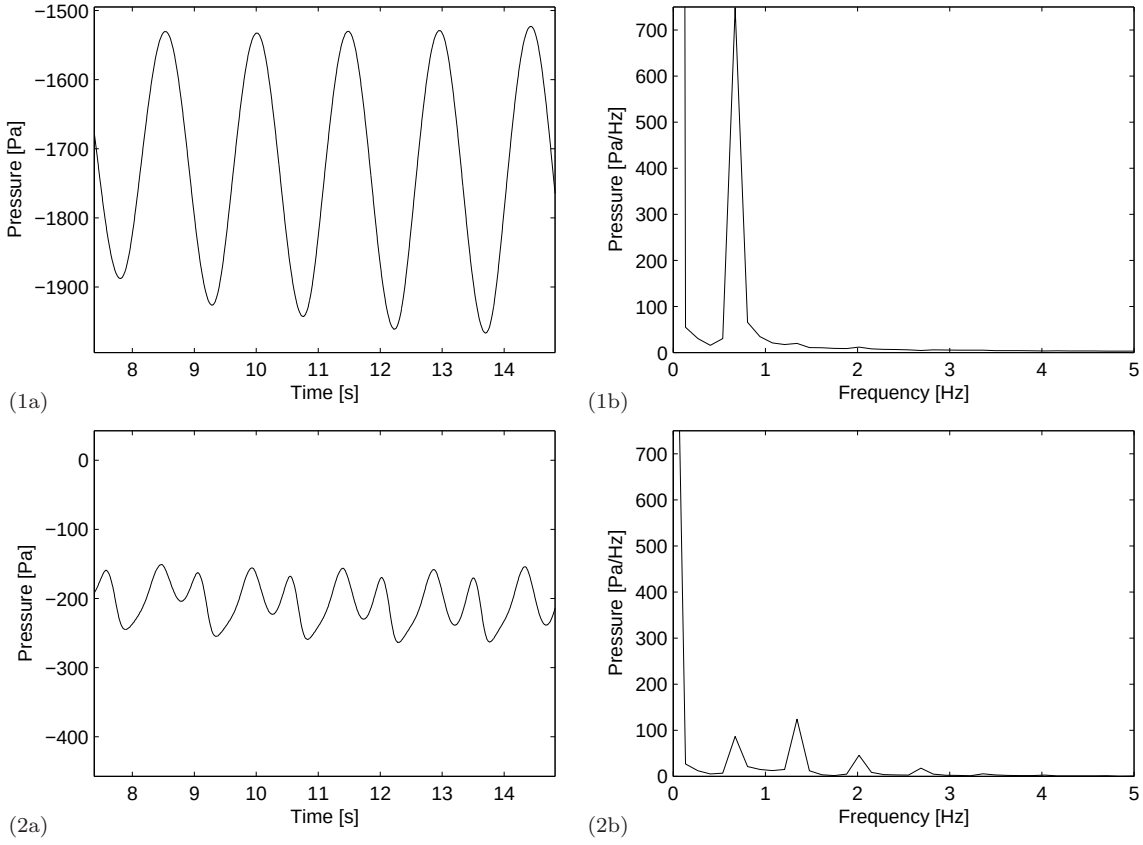

Figure 8: (a) Time history and (b) frequency content of the pressure at the cylinder's surface in the points (1) B and (2) E of the 2 by 2 group.

During the last vortex shedding period, from $t = 13.335\,\mathrm{s}$ to $t = 14.820\,\mathrm{s}$, the time average, the standard deviation and the maxima and minima of the time history of all

degrees of freedom are stored. Figure 9 shows the time average and the standard deviation of the pressure p.

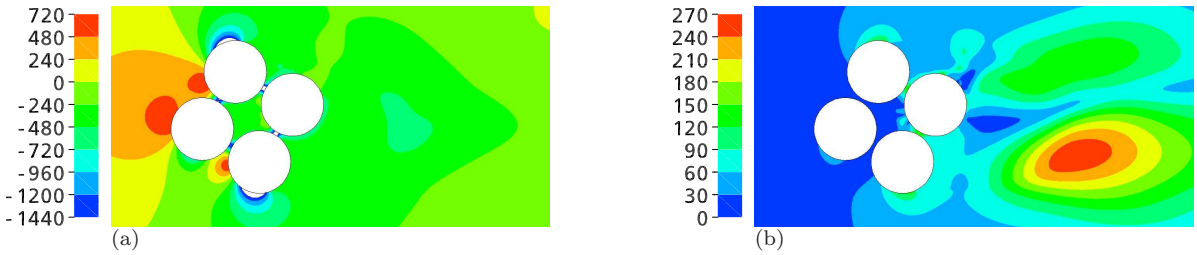

Figure 9: (a) Time average and (b) standard deviation of the pressure p for a transient computation for a 2 by 2 group.

Figure 10 shows the time-averaged pressure coefficients for the flow around the group compared with the pressure coefficient for the flow around a single cylinder. The time average is computed from $t = 7.385\,\mathrm{s}$ to $t = 14.820\,\mathrm{s}$. The group configuration drastically changes the pressure distribution around the cylinders. The value of the stagnation pressure coefficient is almost the same as for the flow around a single cylinder, while high values of suction are present at the location of the small gaps between the cylinders and upstream of the separation points for the cylinders on the side corners of the group (cylinders 2 and 3).

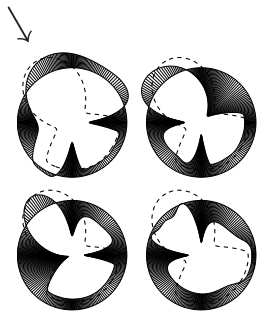

Figure 10: Time-averaged pressure coefficients $\overline{C_p}$ for the flow around a 2 by 2 group (solid line) and for the flow around a single cylinder (dashed line). The arrow indicates the wind direction.

Figure 11a shows the time-averaged drag coefficients for the flow around the group. Cylinder 1, at the head of the group, experiences a higher drag coefficient in comparison with the flow around a single cylinder ($\overline{C_d} = 0.35 - 0.36$). Cylinder 4, in the wake, is pushed towards the other cylinders of the group. The time-averaged lift coefficients $\overline{C_l} = \int_0^{2\pi} \overline{C_p} \sin\alpha d\alpha$ are quite high (figure 11b). The wind pushes the cylinders away from each other.

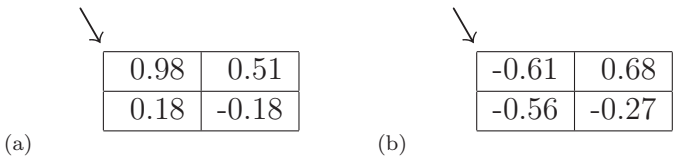

(a) (b)

Figure 11: (a) Time-averaged drag coefficient $\overline{C_d}$ and (b) time-averaged lift coefficient $\overline{C_l}$ for the flow around the 2 by 2 group. The arrow indicates the wind direction.

The time-averaged pressure coefficient is decomposed into a series of cosine functions with circumferential wavenumber n, corresponding to the mode shapes of an axisymmetric structure:

$$\overline{C_p} = \sum_{n=0}^{\infty} \overline{C_p}^n \cos(n\theta + \overline{\varphi}_n) \tag{6}$$

Figure 12 shows a top and a three-dimensional view of the five mode shapes with the lowest eigenfrequencies of the silos in the port of Antwerp[9]. The eigenmodes with $n = 3$ or $n = 4$ have the highest contribution to the response of the silos under wind loading[10].

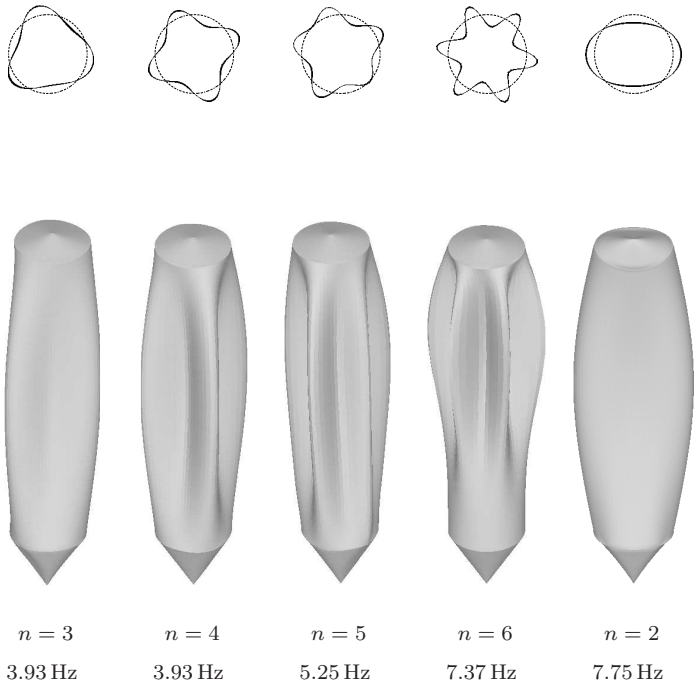

Figure 12: Top and three-dimensional view of the five mode shapes of the silo with the lowest eigenfrequencies.

Figure 13 shows the amplitudes $\overline{C_p}^n$ for the flow around the group for $n = 0-10$, which constitute the major part of the pressure coefficient, compared with the amplitudes for

the flow around a single cylinder. For all values of n, except $n = 2$, larger amplitudes $\overline{C_p}^n$ than for a single cylinder occur for one or more cylinders in the group. For the cylinders on the side corners of the group, the amplitudes $\overline{C_p}^n$ for $n = 3$ and $n = 4$ are larger than the amplitudes for a single cylinder.

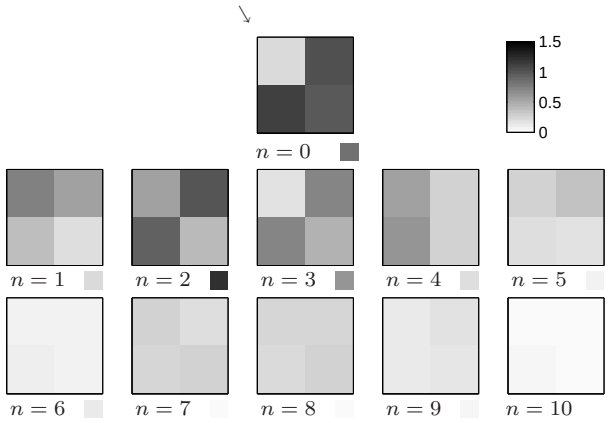

Figure 13: Decomposition of the time-averaged pressure coefficient $\overline{C_p}$ into a series of cosine functions with circumferential wavenumber n for the flow around the 2 by 2 group (2 by 2 squares) and for the flow around a single cylinder (single square). The arrow indicates the wind direction.

For comparison, the flow is computed on a finer mesh, where the nodes next to the cylinder wall lie within the viscous sublayer (figure 14). The mesh consists of 511444 elements and 810088 nodes.

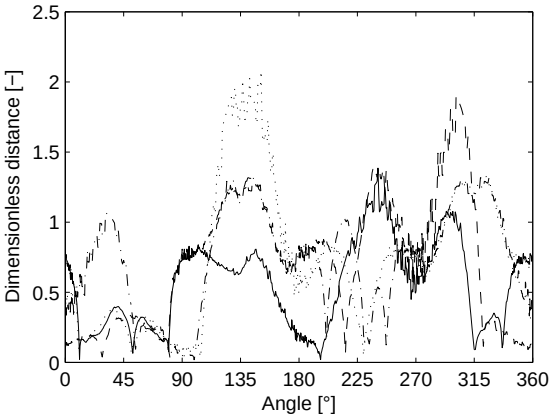

Figure 14: Dimensionless distance y^+ of the nodes next to the cylinder wall as a function of the angle θ for the finer mesh for cylinder 1 (solid line), 2 (dashed line), 3 (dotted line) and 4 (dash-dotted line) of the 2 by 2 group.

1933 time steps are computed, which results in a time window of 9.665 s. Figure 15 compares the time-averaged pressure coefficients on the coarse and the fine mesh as a function of the angle θ for the four cylinders. The minima and maxima are indicated. For the fine mesh the time average is computed from $t = 5.170\,\mathrm{s}$ to $t = 9.665\,\mathrm{s}$. Small differences between both meshes are noticeable, most pronounced at the small gaps and around the separation points.

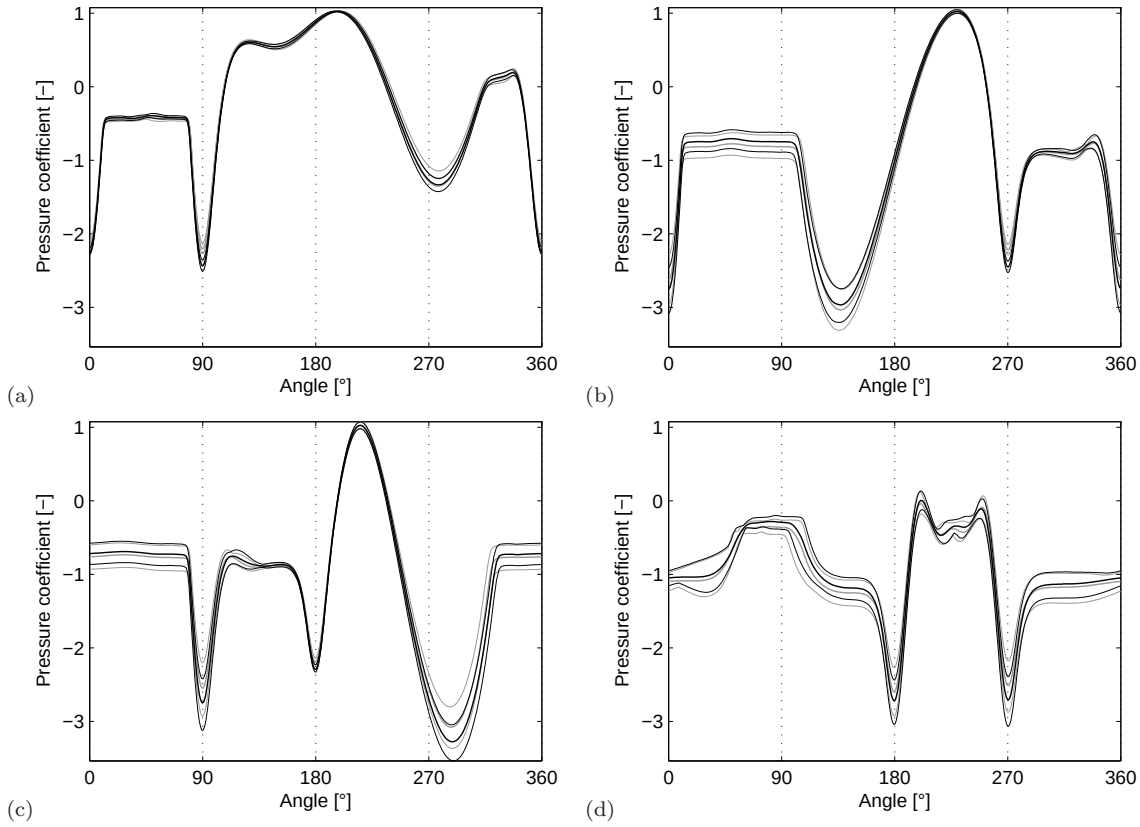

Figure 15: Time average (thick line), maximum and minimum (thin lines) of the pressure coefficient C_p for the coarse (black) and the fine (grey) near-wall mesh as a function of θ for (a) cylinder 1, (b) cylinder 3, (c) cylinder 2 and (d) cylinder 4 of the 2 by 2 group.

3.2 8 by 5 group

Figure 16 shows a detail of the mesh near the group of 8 by 5 cylinders. The mesh consists of 566866 elements and 921438 nodes.

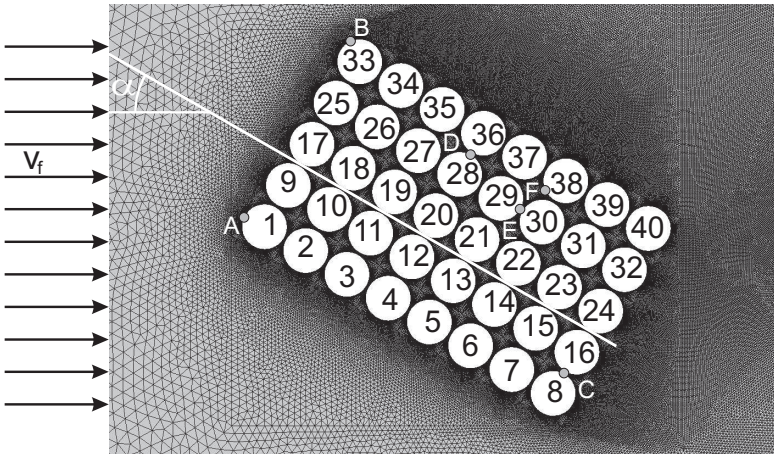

Figure 16: Detail of the mesh for the 8 by 5 cylinder group.

The transient solution is integrated with a time step $\Delta t = 0.01\,\mathrm{s}$. Maximum 10 iterations are performed within every time step to obtain a converged solution. 5170 time steps are computed, which results in a time window of 51.70 s.

Figure 17 shows for the forty cylinders the dimensionless distance y^+ of the nodes next to the cylinder wall as a function of the angle θ at time $t = 51.70\,\mathrm{s}$. Most points lie within the region where the logarithmic law is valid.

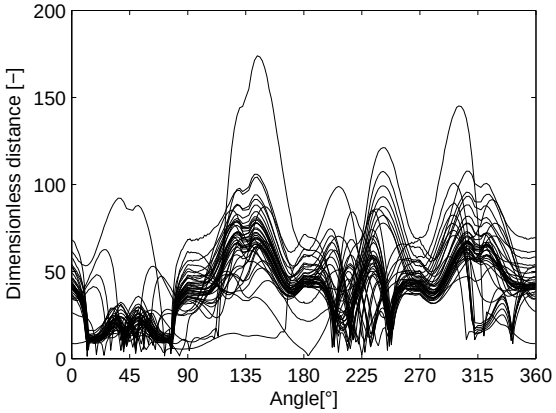

Figure 17: Dimensionless distance y^+ of the nodes next to the cylinder wall as a function of the angle θ for all cylinders of the 8 by 5 group.

Figure 18 shows the time history and the frequency content between $t = 33.48\,\mathrm{s}$ and $t = 51.70\,\mathrm{s}$ of the pressure at the cylinder's surface at a separation point (B) and at a small gap (E), as indicated in figure 16. At the stagnation points, the pressure is constant in time. Generally, the pressure variation on cylinders at the windward side has mainly components around 0.165 Hz, which corresponds to a Strouhal number of 0.24, using the projected width 45.89 m of the group as a characteristic diameter. In the middle of the group and in the wake, there is also an important component at 2.85 Hz. A vortex shedding frequency of 2.85 Hz corresponds to a Strouhal number of 0.49 using the cylinder diameter as a characteristic length. This is consistent with higher Strouhal numbers measured in closely spaced tube arrays[11]. Generally, time variations of the pressure are larger at the leeward side of the cylinder group. The vortex shedding frequencies and Strouhal numbers are quite inaccurate since the frequency resolution $\Delta f = 1/T = 0.055\,\mathrm{Hz}$ is low.

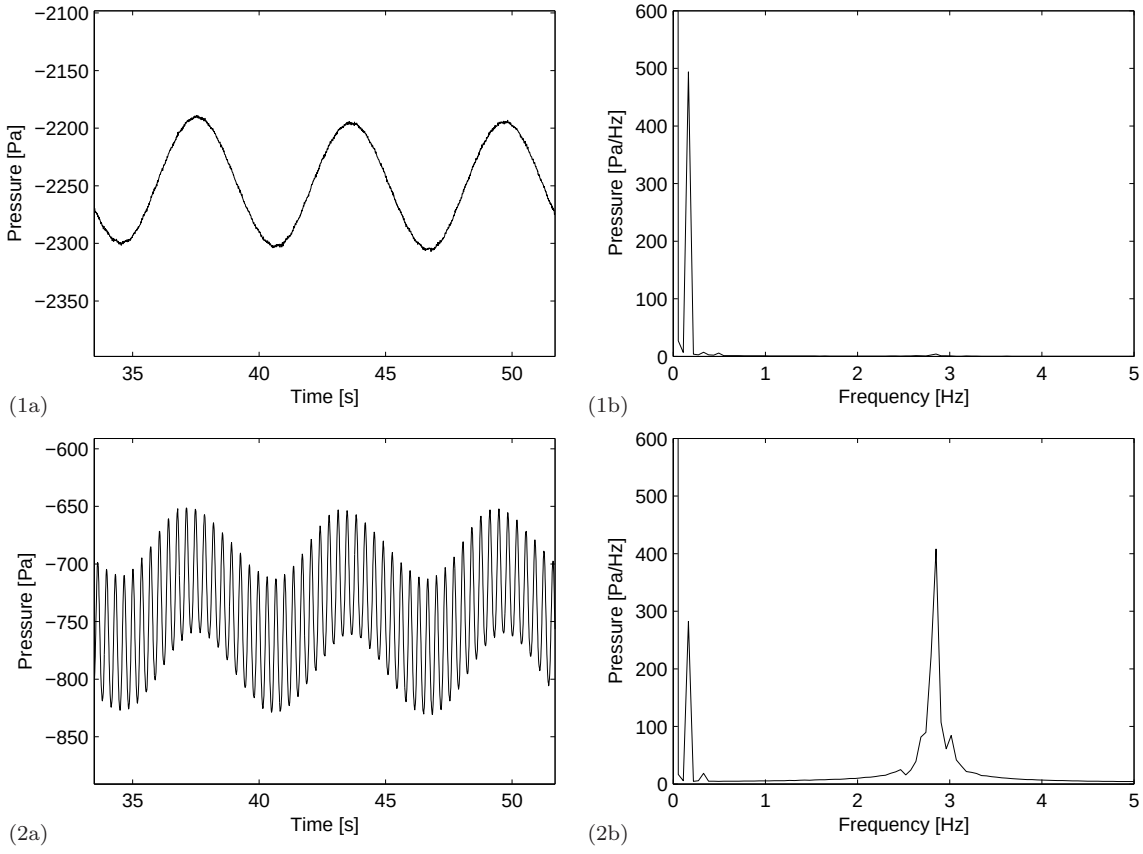

Figure 18: (a) Time history and (b) frequency content of the pressure at the cylinder's surface in the points (1) B and (2) E of the 8 by 5 group.

Figure 19 shows the time average from $t = 39.56\,\mathrm{s}$ to $t = 51.70\,\mathrm{s}$ of the pressure p.

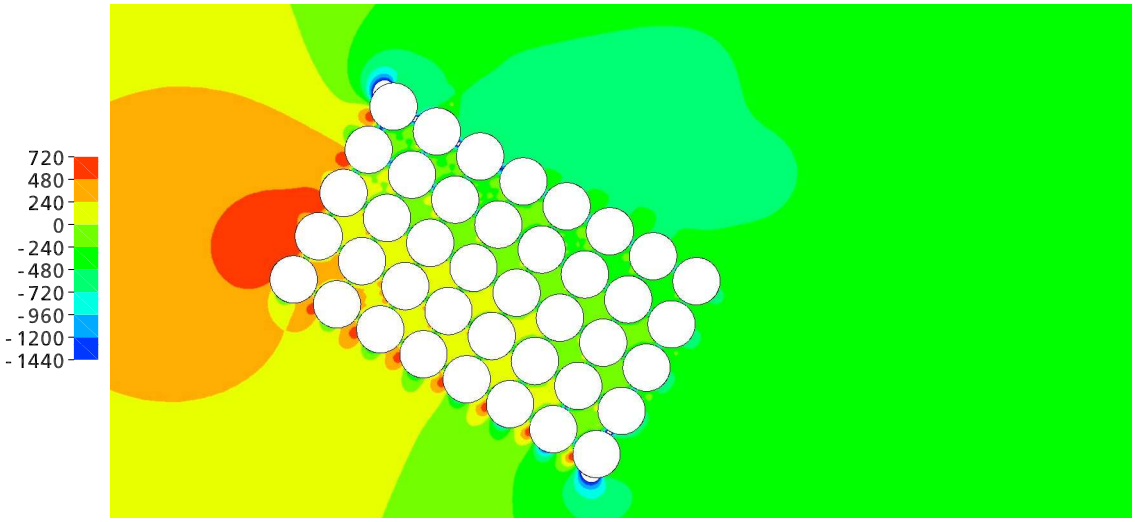

Figure 19: Time average of the pressure p for a transient computation for a 8 by 5 group.

Figure 20 shows the time-averaged pressure coefficients for the flow around the group compared with the pressure coefficient for the flow around a single cylinder. The time average is computed from $t = 33.48\,\mathrm{s}$ to $t = 51.70\,\mathrm{s}$. The group configuration drastically changes the pressure distribution around the cylinders. The value of the stagnation pressure coefficient is almost the same as for the flow around a single cylinder, while high values of suction are present at the location of the small gaps between the cylinders and upstream of the separation points, especially for the cylinders on the side corners of the group (cylinders 8 and 33).

Figure 21a shows the time-averaged drag coefficients for the flow around the group. At the windward side of the group cylinders 9, 17 and 25 experience a higher drag coefficient than for the flow around a single cylinder ($\overline{C_d} = 0.35 - 0.36$), while in the middle of the group the drag coefficients are considerably lower. At the two side corners (cylinders 8 and 33) the drag coefficient is also low. Figure 21b shows the time-averaged lift coefficients. The cylinders on the borders of the group are pushed away from the group, which results in quite high lift coefficients for these cylinders, especially for the two on the side corners (cylinders 8 and 33).

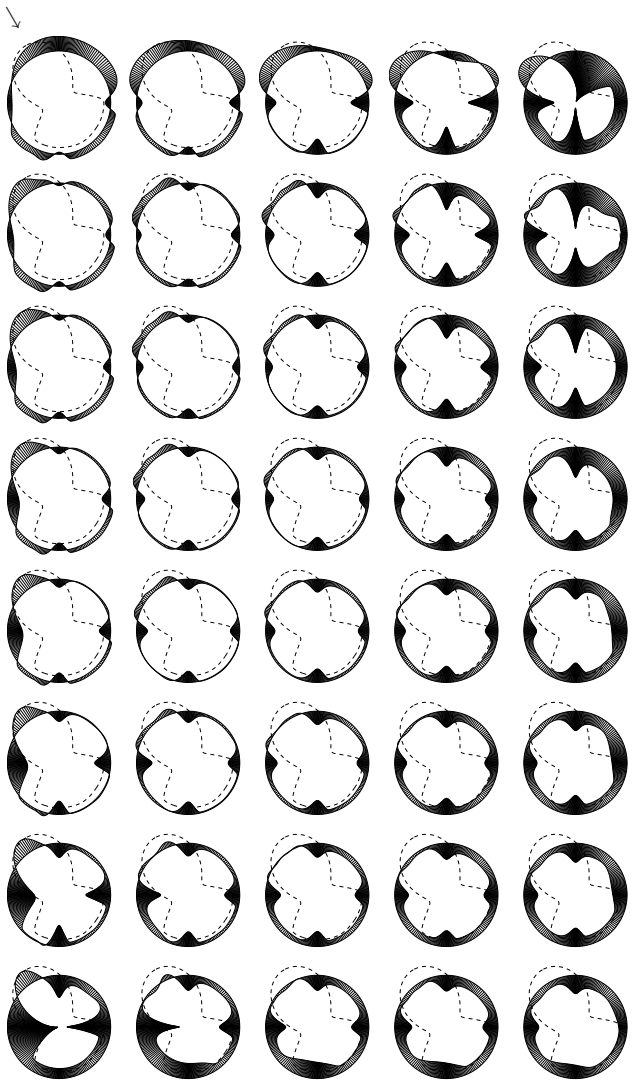

Figure 20: Time-averaged pressure coefficients $\overline{C_p}$ for the flow around a 8 by 5 group (solid line) and for the flow around a single cylinder (dashed line). The arrow indicates the wind direction.

As above, the time-averaged pressure coefficient is decomposed into a series of cosine functions with circumferential wavenumber n. Figure 22 shows the amplitude $\overline{C_p}^n$ for the flow around the group for $n = 0 - 10$, compared with the amplitudes for the flow around a single cylinder. For all values of n, except $n = 2$, larger amplitudes $\overline{C_p}^n$ than for the flow around a single cylinder occur for one or more cylinders in the group. The highest values are always situated on the borders of the group.

(a)

0.27	0.61	0.67	0.74	0.13
0.05	0.16	0.19	0.21	0.16
0.05	0.16	0.16	0.15	0.15
0.03	0.13	0.14	0.09	0.01
0.03	0.13	0.15	0.14	0.19
0.06	0.13	0.15	0.14	0.17
0.16	0.13	0.15	0.12	0.14
0.20	0.27	0.34	0.22	0.02

(b)

-0.50	-0.22	-0.13	0.01	1.01
-0.06	0.14	0.23	0.37	0.22
-0.09	0.08	0.21	0.31	0.22
-0.14	0.08	0.16	0.25	0.52
-0.20	0.05	0.14	0.16	0.37
-0.27	-0.02	0.10	0.13	0.30
-0.36	-0.16	0.04	0.09	0.23
-0.84	-0.69	-0.19	-0.09	0.00

Figure 21: (a) Time-averaged drag coefficient $\overline{C_d}$ and (b) time-averaged lift coefficient $\overline{C_l}$ for the flow around the 8 by 5 group. The arrow indicates the wind direction.

For all multiples of 4, $\overline{C_p}^n$ has a larger amplitude for almost all cylinders of the group due to its configuration (four small gaps surround each cylinder). Especially for the cylinders on the side corners of the group, the amplitudes $\overline{C_p}^n$ for $n = 3$ and $n = 4$ are larger than the amplitudes for the flow around a single cylinder.

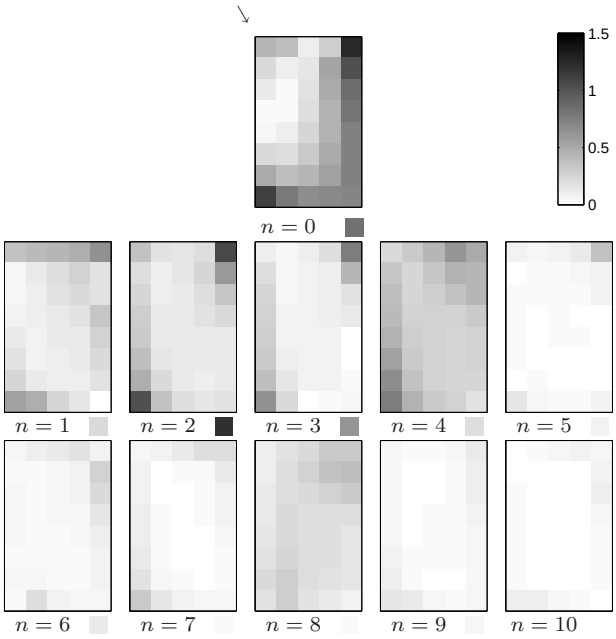

Figure 22: Decomposition of the time-averaged pressure coefficient $\overline{C_p}$ into a series of cosine functions with circumferential wavenumber n for the flow around the 8 by 5 group (8 by 5 squares) and for the flow around a single cylinder (single square). The arrow indicates the wind direction.

4 CONCLUSIONS

In this paper, the results of the Reynolds Averaged Navier Stokes simulation of the post-critical flow around a single circular cylinder and groups of cylinders are reviewed.

First, the transient 2D turbulent air flow around a single cylinder at $\mathrm{Re} = 1.24 \times 10^7$ is computed using the SST turbulence model and the results are compared with the pressure coefficients of Eurocode 1 and with experimental data. The mesh refinement close to the wall has only a small influence on the pressure coefficient. The minimum pressure coefficient is underestimated, while the base pressure coefficient is slightly overestimated.

Unsteady simulations are performed for the flow around a group of 2 by 2 and of 8 by 5 cylinders. The group configuration drastically changes the pressure distribution around the cylinders.

The largest time variations of the pressure coefficient occur at the leeward side of the groups. For the 2 by 2 group, the vortex shedding frequency is equal to 0.67 Hz and higher harmonics are present at the leeward side of the group. For the 8 by 5 group, vortices shed at 0.165 Hz from the group as a whole and at 2.85 Hz from the individual cylinders.

The time-averaged pressure coefficient at the stagnation points is almost the same as for the flow around a single cylinder, while high values of suction are present at the location of the small gaps between the cylinders and upstream of the separation points, especially for the cylinders on the side corners of the groups.

At the windward side of the groups, some cylinders experience a higher drag coefficient than for the flow around a single cylinder, while in the middle of the 8 by 5 group the drag coefficients are considerably lower. The lift coefficients for the cylinders on the borders of the groups are quite high, especially for the two cylinders on the side corners.

The time-averaged pressure coefficient is decomposed into a series of cosine functions with circumferential wavenumber n, corresponding to the mode shapes of an axisymmetric structure. For the silos in the port of Antwerp, eigenmodes with $n = 3$ or $n = 4$ have the lowest eigenfrequency and the highest contribution to the response of the silos under wind loading. The highest values of a projection $\overline{C_p}^n$ are always situated on the borders of the group. For all multiples of 4, $\overline{C_p}^n$ has a larger amplitude for almost all cylinders of the group than for the flow around a single cylinder due to the configuration of the group (four small gaps surround each cylinder). Especially for the cylinders on the side corners of the group, the amplitudes $\overline{C_p}^n$ for $n = 3$ and $n = 4$ are larger.

ACKNOWLEDGMENTS

The authors gratefully acknowledge the support of Ellimetal n.v. for this research.

References

[1] Belgisch Instituut voor Normalisatie. *NBN ENV 1991-2-4: Eurocode 1: Grondslag voor ontwerp en belasting op draagsystemen - Deel 2-4 : Belasting op draagsystemen - Windbelasting*, November 1995.

[2] F.R. Menter. Two-equation eddy-viscosity turbulence models for engineering applications. *AIAA Journal*, 32(8):1598–1605, 1994.

[3] Ansys, Inc. *Ansys CFX version 5.7.1*, November 2004.

[4] M.M. Zdravkovich. *Flow around circular cylinders. Vol 1: Fundamentals*. Oxford University Press, 1997.

[5] D. Dooms, G. De Roeck, and G. Degrande. Reynolds Averaged Navier Stokes simulation of the post-critical flow around a single circular cylinder and groups of cylinders. In *Proceedings of the 7th National Congress on Theoretical and Applied Mechanics*, Mons, Belgium, May 2006. National Committee for Theoretical and Applied Mechanics.

[6] M. Behr, D. Hastreiter, S. Mittal, and T.E. Tezduyar. Incompressible flow past a circular cylinder: Dependence of the computed flow field on the location of the lateral boundaries. *Computer Methods in Applied Mechanics and Engineering*, 123:309–316, 1995.

[7] M. Behr, J. Liou, R. Shih, and T.E. Tezduyar. Vorticity streamfunction formulation of unsteady incompressible flow past a cylinder : Sensitivity of the computed flow field to the location of the outflow boundary. *International Journal for Numerical Methods in Fluids*, 12:323–342, 1991.

[8] G. Iaccarino, A. Ooi, P.A. Durbin, and M. Behnia. Reynolds averaged simulation of unsteady separated flow. *International Journal of Heat and Fluid Flow*, 24(2):147–156, 2003.

[9] D. Dooms, G. Degrande, G. De Roeck, and E. Reynders. Finite element modelling of a silo based on experimental modal analysis. *Engineering Structures*, 28(4):532–542, 2006.

[10] D. Dooms, S. Jacobs, G. Degrande, and G. De Roeck. Dynamische analyse van een groep silo's onder dynamische windbelasting: In situ metingen op een lege hoeksilo. Report to Ellimetal BWM-2003-09, Department of Civil Engineering, K.U.Leuven, June 2003.

[11] R.D. Blevins. *Flow induced vibration*. Van Nostrand Reinhold, 1977.